Peripheral positioning of lysosomes supports melanoma aggressiveness

K. Jerabkova-Roda, A. Mousson, M. Peralta, R. Karali, H. Justiniano, L.M. Lisii, P. Carl, N. Asokan, I. Busnelli, A. Larnicol, et al.

Peripheral positioning of lysosomes supports melanoma aggressiveness

K. Jerabkova-Roda[1-5@], A. Mousson[2,6], M. Peralta[1-4], R. Karali[2,6], H. Justiniano[2,6], L.M. Lisii[2,6], P. Carl[2,6], N. Asokan[1-4], I. Busnelli[1-4], A. Larnicol[1-4], O. Lefebvre[1-4], H. Lachuer[5,£], A. Pichot[2,3,8], T. Stemmelen[2,3,8], A. Molitor[2,3,8,9], A. Hirschler[10], F. Delalande[10], E. Sick[2,6], R. Carapito[2,3,8,9], C. Carapito[10], V. Hyenne[1-4,11*], K. Schauer[5,7*@], P. Rondé[2,6*@], and J.G. Goetz[1-4*@]

[1]Tumor Biomechanics, INSERM UMR$_S$1109, $Strasbourg, France$
[2]Université de Strasbourg, Strasbourg, France
[3]Fédération de Médecine Translationnelle de Strasbourg (FMTS), Strasbourg, France
[4]Équipe labellisée Ligue Contre le Cancer
[5]Institut Curie, PSL, CNRS, UMR144, Paris, France
[6]CNRS UMR7021, Faculté de Pharmacie, Illkirch, France
[7]Institut Gustave Roussy, INSERM UMR1279, Université Paris-Saclay, Villejuif, France
[8]Plateforme GENOMAX, Institut thématique interdisciplinaire (ITI) de Médecine de Précision de Strasbourg Transplantex NG, Fédération Hospitalo-Universitaire OMICARE
[9]Service d'Immunologie Biologique, Plateau Technique de Biologie, Pôle de Biologie, Nouvel Hôpital Civil, Hôpitaux Universitaires de Strasbourg, 1 Place de l'Hôpital, 67091, Strasbourg, France
[10]CNRS, Laboratoire de Spectrométrie de Masse Bio-Organique (LSMBO), IPHC, UMR 7178, Université de Strasbourg, Strasbourg 67087, France
[11]CNRS SNC5055, Strasbourg, France
[1]Current address : Université de Paris, CNRS, Institut Jacques Monod, 75013 Paris, France
[*]Equal contribution
[@]Corresponding authors

Emerging evidences suggest that both function and position of organelles are pivotal for tumor cell dissemination. Among them, lysosomes stand out as they integrate metabolic sensing with gene regulation and secretion of proteases. Yet, how the function of lysosomes is linked to their position and how this controls metastatic progression remains elusive. Here, we analyzed lysosome subcellular distribution in micropatterned patient-derived melanoma cells and found that lysosome spreading scales with their aggressiveness. Peripheral lysosomes promote invadopodia-based matrix degradation and invasion of melanoma cells which is directly linked to their lysosomal and cell transcriptional programs. When controlling lysosomal positioning using chemo-genetical heterodimerization in melanoma cells, we demonstrated that perinuclear clustering impairs lysosomal secretion, matrix degradation and invasion. Impairing lysosomal spreading in a zebrafish metastasis model significantly reduces invasive outgrowth. Our study provides a mechanistic demonstration that lysosomal positioning controls cell invasion, illustrating the importance of organelle adaptation in carcinogenesis.

Keywords: lysosome, invasion, metastasis

Correspondence: ***katerina.jerabkova@inserm.fr*** ***kristine.schauer@gustaveroussy.fr*** ***philippe.ronde@unistra.fr*** ***jacky.goetz@inserm.fr***

Main

Metastases are responsible for the majority of cancer-related deaths (Dillekås et al., 2019). Melanoma shows strong negative correlation between cancer stage and 5-year patient survival, making it an ideal model to study phenotypic changes leading to cancer cell invasion, adaptation and survival. Melanoma progression consists of multiple sequential events. First, melanocytes are transformed and grow in the epidermis during radial growth phase (RGP), forming a premalignant lesion. Changes in their transcription program lead to expression of matrix-degrading enzymes and to invasion through the dermis during vertical growth phase (VGP) followed by cancer dissemination through vascular and lymphatic routes, progressing into metastatic stages (Braeuer et al., 2011). To colonize secondary organs during metastasis, melanoma cells sense their microenvironment and react by locally degrading and remodeling the extracellular matrix (ECM). Invading melanoma cells frequently form dynamic actin-rich protrusive structures with high proteolytic activity, called invadopodia, that mediate ECM degradation (Augoff et al., 2020), . Invadopodia formation involves the local docking of endosomal compartments, such as multivesicular bodies, and their fusion with the plasma membrane (Hoshino et al., 2013). This suggests that melanoma metastasis requires specific invasion programs for an efficient and targeted delivery of ECM-degrading enzymes to highly-specialized structures. Yet how this is orchestrated in invasive cells remains unclear. Over the past decade, several reports indicated that lysosomes constitute novel regulators of invasion by allowing cells to sense their microenvironment and trigger adapted responses, notably through the exocytic release of their content (Ballabio and Bonifacino, 2020). For instance, lysosomal exocytosis drives the formation of invasive protrusions resulting in basement membrane breaching in C. elegans (Naegeli et al., 2017). In addition, secretion of lysosomal cathepsin B promotes cancer cell invasion and metastasis (Bian et al., 2016). Besides, lysosome secretion contributes to the repair of plasma membrane damages occurring during cell migration and results in better cell survival under mechanical stress (Corrotte and Castro-Gomes, 2019). Importantly, lysosomal activity is regulated by their subcellular location (Johnson et al., 2016; Korolchuk et al., 2011). Peripheral lysosomes are prone to exocytosis and drive growth factor signaling (Jia and Bonifacino, 2019), while perinuclear lysosomes have a decreased pH and higher proteolytic activity (Johnson et al., 2016). Lysosome distribution is in turn directly impacted by the cellular microenvironment (Steffan et al., 2009). Lysosomes are transported to the plasma membrane via kinesins

(anterograde transport) in response to growth factors and nutrients presence, conversely, during starvation and in alkaline environment, lysosomes are transported to the perinuclear region (retrograde transport) in a dynein-dependent manner (Ballabio and Bonifacino, 2020). While the molecular mechanisms driving lysosomal positioning have been partially elucidated, it remains unclear whether it can control invasion programs of melanoma cells. A parallel study by Marwaha and colleagues (Marwaha et al., 2023) demonstrates that peripheral lysosomes control the emergence of leader cells during epithelial collective migration events, suggesting that lysosomal positioning is likely a universal mechanism controlling cell invasion within tissues. Here, we investigated how lysosome dynamics contribute to cancer aggressiveness and metastatic progression. We reveal a phenotypic switch concerning lysosome positioning in aggressive melanoma that is supported by distinct transcriptional programs and controls migration and invasion. Our study illustrates the importance of organelle adaptation in carcinogenesis by providing mechanistic evidences that lysosomal positioning controls secretory pathways of malignant transformation.

Melanoma invasiveness scales with lysosome spreading Cells progressing through the metastatic cascade display tremendous phenotypic plasticity in the benefit of increased invasion and ECM degradation potential. Transition of melanoma cells from RGP to VGP involves a series of invasion-promoting programs, particularly the concerted expression of matrix-degrading enzymes (Braeuer et al., 2011) and the maturation of invadopodia (Weidmann et al., 2016). In order to investigate which organelles control such invasion-promoting programs, we first characterized the invasive properties of a collection of patient-derived melanoma cells from different stages (RGP: WM1552c, WM1862, VGP: WM115, WM983A and metastatic: WM983B, A375 cells). Using collagen invasion assay (Fig 1a), we identified three patient-derived cell lines with low, medium and high invasion potential (Fig 1b,c), which correlated with their cancer progression state (RGP, VGP, metastatic). Using gelatin degradation assay (Fig 1d), we further showed that cells with high invasion index displayed significantly increased gelatin degradation frequency and area (Fig 1e,f) confirming previous observations (Mousson et al., 2021). Notably, gelatin degradation areas were mainly located at invadopodia identified by the invadopodia markers, actin and cortactin (Fig 1e). Because ECM degradation is mostly mediated by enzymes, such as metalloproteases (MMPs) or cathepsins, contained in lysosomes, and released by exocytosis at invadopodia (Jacob and Prekeris, 2015), we tested whether lysosomal marker LAMP1 co-localizes with active invadopodia. We found that LAMP1 colocalized with actin and cortactin in a subset of degradation areas (Fig S1 a-d) suggesting at least transient presence of lysosomes at podosomes as reported previously in v-Src transformed fiboblasts (Tu et al., 2008). We accessed transcriptional programs of the three representative patient-derived cell lines with graded invasion index (WM1862, WM983A, WM983B) using RNAseq and Gene Ontology analysis. This showed an overrepresentation of metabolism, actin cytoskeleton and cell migration pathways associated with a concomitant reduction of transcripts linked to the lysosomal pathway (Fig.1g and Table 1). We thus hypothesized that increased invasion occurs through a phenotypic switch from a lysosomal signature characteristic of RGP cells (WM1862) to a migratory signature found in metastatic cells. We next investigated the sub-cellular localization of LAMP1, a marker of late endosomes and lysosomes (referred to as lysosomes hereafter) in these cell lines. Micropatterning allows for high-throughput study of cells with reproducible shapes (Fig 1h) and facilitates the comparison and quantitative positional analysis of lysosomes in 2D (Figure 1i) or in full cell volume (Figure 1j). While RGP cells had mostly perinuclear lysosomes, metastatic cells showed significant dispersion of LAMP1-compartments towards the cell periphery (Fig 1h-j) characterized by a significant increase in the mean inter-organelle distance and the mean distance to the barycenter (Figure 1k,l). Moreover, LAMP1-compartments were smaller and more numerous in metastatic cells (Fig S1e,f), revealing that the observed transcriptional changes in melanoma cells correlate with changes in LAMP1 distribution. Our results identify and characterize a remarkable cellular phenotype of scattered lysosomes associated with aggressive malignancy in melanoma. Since peripheral lysosome positioning has been reported earlier in other cancer types (breast cancer (Ping-Hsiu Wu et al., 2020) and bladder cancer (Mathur et al., 2023)), it is tempting to speculate that peripheral lysosome repositioning could represent a universal feature of cancer progression. Indeed, our transcriptomics data demonstrate that genes known to promote perinuclear localization of lysosomes, such as RILP (Pu et al., 2016) or RNF167 (Nair et al., 2020), show decreased expression, and conversely, genes linked to anterograde transport, such as KIF1B and KIF5B (Moamer et al., 2019), are overexpressed in metastatic cells. Interestingly, lysosomal genes previously associated with cancer progression such as LAMP1 (Machado et al., 2015; Wang et al., 2017), lysosomal Ca2+ channel MCOLN1 (Medina et al., 2011) and several MMPs (Hua et al., 2011) (MMP2, MMP15, MMP16, MMP17) are upregulated in metastatic cells, besides an overall loss of lysosomal signature in these cells. Yet, lysosomal dispersion could be uncoupled from lysosome biogenesis as some studies report its induction in highly metastatic breast cancer cells (Glunde et al., 2003) or during pancreatic ductal adenocarcinoma progression (Perera et al., 2015). Further work is therefore needed to identify what are the molecular programs controlling the positioning and the biogenesis of lysosomes in invasive melanomas cells and what triggers their activation.

Forcing lysosome perinuclear clustering in melanoma cells We next engineered melanoma cells employing a chemo-genetic strategy based on the heretodimerization of the FKBP-FRB domains by Rapalog or derivatives (Kapitein et al., 2010) for lysosome positioning control. We chose WM983A and WM983B cell lines, derived from the primary tumor and metastatic site of the same patient, respectively.

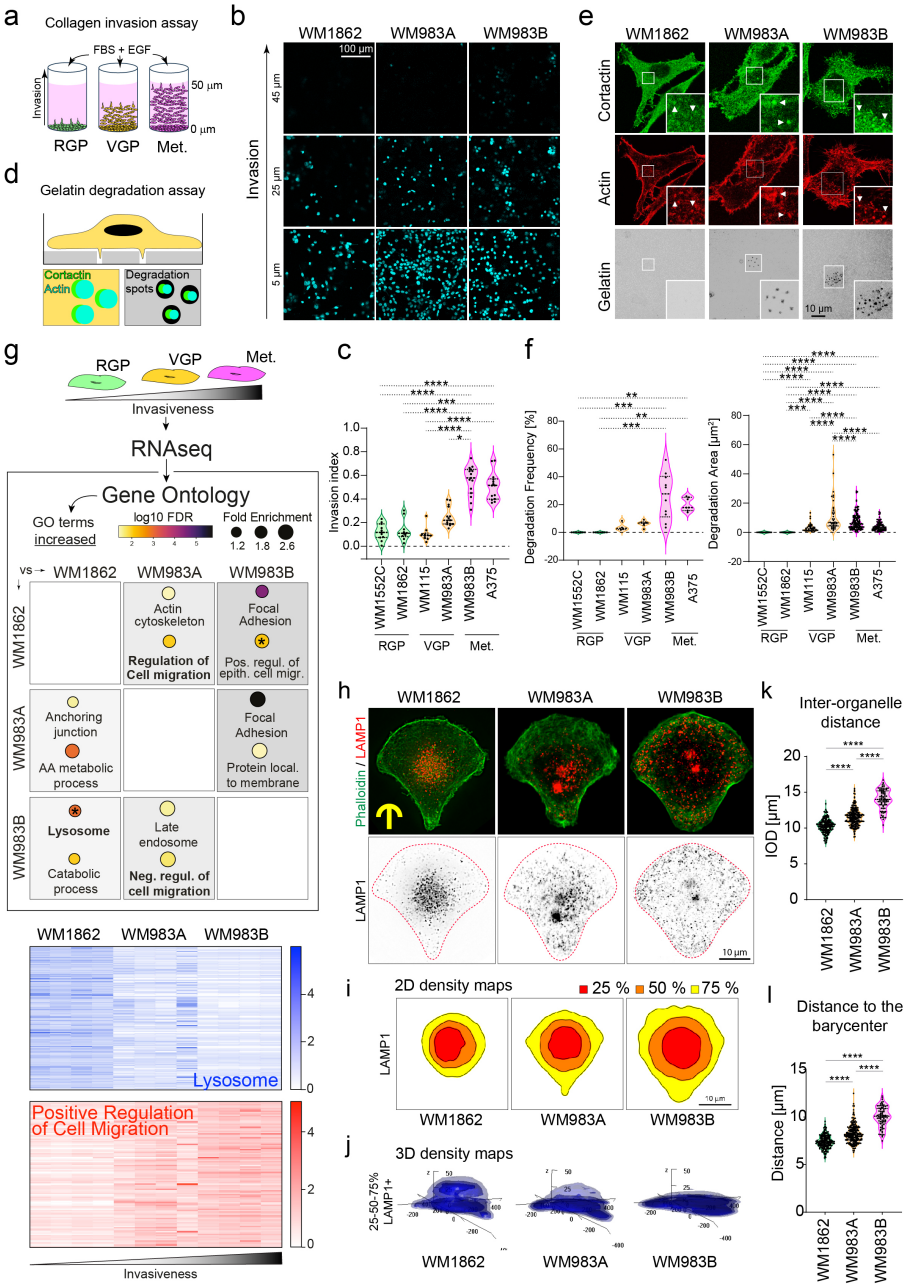

Fig. 1. Melanoma invasiveness correlates with lysosome spreading a-c) Invasive potential of human melanoma cells (WM1552c, WM1862, WM115, WM983A, WM983B, A375) was analyzed using collagen invasion assay. b) Cells were seeded into a collagen plug, cultured for 24 hours and their spreading at distance of the seeding position was analyzed by confocal imaging. c) For each cell line, the invasion index equals the number of nuclei above 10 µm distance divided by the total number of cells. Invasion index (Mean ± SD) = 0.1213 ± 0.070, 0.1334 ± 0.089, 0.2500 ± 0.080, 0.1036 ± 0.060, 0.5562 ± 0.125, 0.5070 ± 0.117, respectively, in triplicate, one dot represents 1 field of view. Kruskal-Wallis with Dunn's multiple comparison post-hoc test. d-f) Degradation capacity of the melanoma cell lines was assessed using gelatin degradation assay allowing to visualize actin, cortactin and degradation spots. e) Cells were seeded on FITC-gelatin for 24 hours, fixed and stained with Cortactin antibody and Phalloidin to label invadopodia and imaged using confocal microscopy. f) Degradation frequency (DF) was calculated as a percentage of cells displaying gelatin degradation activity. DF (Mean ± SD) = 0.00, 0.00, 6.19 ± 2.26, 4.00 ± 2.94, 26.08 ± 16.52, 20.08 ± 4.79, respectively, in triplicate one dot represents 1 field of view. For cells displaying degradation activity, the degradation area (DA, total area per cell) was quantified. DA (Mean ± SD) = 0.00, 0.00, 11.13 ± 11.00, 3.19 ± 2.76, 7.48 ± 5.59, 3.99 ± 2.97, respectively, in triplicate one dot represents 1 cell. Kruskal-Wallis with Dunn's multiple comparison post-hoc test. g) Transcriptomics analysis of WM1862, WM983A and WM983B cell lines was performed in quadruplicate, genes showing statistically significant differential expression (pAdj<0,01) were analyzed using gene ontology (GO). Selected GO terms of differentially regulated pathways are listed showing their fold enrichment and log10 FDR in paired comparisons (left panel) and heatmaps are shown for the two main pathways identified (right panel). h-j) WM1862, WM983A, WM983B cells were analyzed using micropatterning. Cells were seeded on 36µm crossbow micropatterns, let spread for 4 hours, fixed and stained with LAMP1 antibody and cell spreading was controlled by actin staining (Phalloidin). 2D (i) and 3D (j) density maps of LAMP1 staining were calculated using R software, displaying the smallest area that can be occupied by 25, 50 and 75per cent of all compartments. k) Inter-organelle distance (IOD) represents average of distances between all lysosomes. IOD (Mean ± SD) = 10.30 ± 0.94, 11.56 ± 1.15, 13.99 ± 1.40, respectively. One dot represents 1 cell. l) Distance to barycenter (DB) represents the distance from each lysosome to the center of mass. DB (Mean ± SD) = 7.40 ± 0.69, 8.21 ± 0.93, 10.03 ± 1.07, respectively. One dot represents 1 cell. Kruskal-Wallis with Dunn's multiple comparison post-hoc test. (i,j,k,l) WM1862, n= 182 cells, WM983A, n= 231 cells, WM983B, n= 82 cells, in triplicate.*p<0,05; ** p<0,01; *** p<0,001; **** p<0,0001.

We stably expressed FKBP domain fused to LAMP1 and the FRB domain fused to dynein adaptor BicD2. Rapalog treatment forced binding of BicD2 and recruitment of Dynein to LAMP1 for the movement towards the minus end of microtubules, and thus perinuclear clustering of the LAMP1 compartment around the microtubule organizing center (Fig. 3a, S2d). Clustering was fast, dose-dependent (Figure 2a,b) and persistent in time (Figure 2b, c, Figure S2c), as previously described (Kapitein et al., 2010), allowing precise control of lysosomal positioning in vitro and in vivo investigations. Engineered control cells expressing only single domain FKBP (FKBP only) did not display lysosome clustering upon Rapalog treatment (Fig 2b, c, S2A). Correlative light and electron microscopy (CLEM) of control- or Rapalog-treated WM983B-LAMP1-mCherry cells showed colocalization between LAMP1-mCherry and vesicular compartments, which clustered as expected in the perinuclear region upon Rapalog treatment (Fig 2d). Notably, Rapalog had no effect on the colocalization between LAMP1-mCherry and the BODIPY-Pepstatin A (Fig S2e), which is delivered to lysosomes via endocytic pathway (Chen et al., 2000) and binds to the active site of cathepsin D under acid condition. Thus, clustering by Rapalog did not disrupt cargo delivery and lysosomal catabolic activity in melanoma cells, indicating that we could control lysosomal positioning in relevant patient-derived cell lines, without interfering with basic lysosomal functions. While our study exploited a chemo-genetic model of forced lysosome clustering, the study by (Marwaha et al., 2023) built on the induction of lysosomal spreading demonstrating that fine control or organelle positioning is now at reach. Both approaches require cell engineering and would benefit from the complementary use of small molecules that regulate lysosome positioning, particular for clinical applications. We previously identified PI3K inhibitors as potent lysosome clustering agents in bladder cancer (Mathur et al., 2023). Indeed, lysosome positioning, and more general organelle topology (Wang et al., 2023), were used as a readout in a screen for novel therapeutic drugs and targets (Circu et al., 2016). This opens an exciting area of research leading to a wider drug discovery approach centered on organelle positioning.

Peripheral lysosomes promote secretion and matrix degradation Lysosome exocytosis of different proteases and subsequent extracellular matrix degradation promotes invasion to adjacent tissues (Monteiro et al., 2013; Naegeli et al., 2017). We thus first investigated how altering positioning of the LAMP1 compartment impacts the cell secretome. We analyzed the concentrated cell supernatant of WM983B cells in the presence and absence of Rapalog treatment (Fig 3a) by mass spectrometry and identified a significant decrease of several lysosome-associated proteins upon clustering (Fig 3a), including Cathepsins. These enzymes contribute to ECM degradation (Vidak et al., 2019) and have been linked with metastatic progression, for instance in the case of Cathepsin S or B in gastric and colorectal cancers respectively (Bian et al., 2016; da Costa et al., 2020). To confirm that clustering inhibits lysosome secretion, we imaged VAMP7-pHluorin, a v-SNARE involved in the fusion of lysosome with plasma membrane (Chaineau et al., 2009) using TIRF microscopy (Fig 3b). We mixed cells expressing either FKBP only or FKBP-FRB and treated them with 25nM Rapalog (Fig 3c). Cells with clustered LAMP1 compartment showed significantly reduced numbers of VAMP7 secretory events (Fig 3d left, Fig 3e), with no impact on the duration of the secretion process (Fig 3d right). Together, these experiments demonstrated that perinuclear localization of lysosomes strongly decreased lysosome secretion in melanoma cells. These results are in line with a previous observation of peripheral lysosomes promoting their fusion with plasma membrane and thus exocytosis in a model of lysosomal storage disease (Medina et al., 2011). Next, we investigated whether lysosome clustering impairs invadopodia-based ECM degradation (Fig 3f). In both cell lines (WM983A, WM983B), we observed a significant decrease in the degradation area (Fig 3g top) upon LAMP1-clustering. While degradation frequency in VGP WM983A cells remained unaltered, metastatic WM983B cells showed a significant decrease (Fig 3g bottom). These results further confirmed that peripheral lysosome positioning promotes lysosome exocytosis and ECM degradation. Forcing perinuclear lysosome localization rescues this phenotype, suggesting that that lysosome position and subsequent secretion promotes ECM remodeling, feature often seen in aggressive cancers (Winkler et al., 2020). More globally, cancer cell secretion is likely to further shape pro-metastatic features of the tumor microenvironment, and favor the emergence of, for example, cancer associated fibroblasts, whose ECM remodeling expertise is pivotal during tumor progression (Kalluri, 2016; Sahai et al., 2020) Our results further suggest that the formation of functional invadopodia requires local lysosome exocytosis. Similarly, targeted secretion of CD63-positive multi-vesicular bodies promotes invadopodia formation. Indeed, other secretory organelles are relocalized to the cell periphery and protrusive structures, and favor, for example, the secretion of pro-tumorigenic extracellular vesicles (Ghoroghi et al., 2021) as it has been shown for CD63+ endo/lysosomes (Hoshino et al., 2013). Whether distinct types of late endosomes act in concert to favor invadopodia-mediated ECM degradation, or whether it involves hybrid late endo-lysosome compartments remains to be determined.

Forcing lysosomal clustering impairs invasion potential of melanoma cells Building on the stability of Rapalog-mediated lysosomal clustering in patient-derived cells and the demonstration that it impairs ECM degradation, we sought to monitor if lysosome position impacted the cancer cell dissemination in vivo. To do so, we intravenously injected melanoma cells with different clustering status in two days post-fertilization (dpf) zebrafish embryos (Follain et al., 2018) to probe lysosomal clustering while assessing the metastatic and invasive potential of melanoma cells over time (Fig 4a). Rapalog treatment (5nM) had no effect on cell proliferation or cell viability (Fig S3a, b) during the 3-days time course. Lysosome clustering was stable in vivo and visible in round circulating tumor cells that had just performed

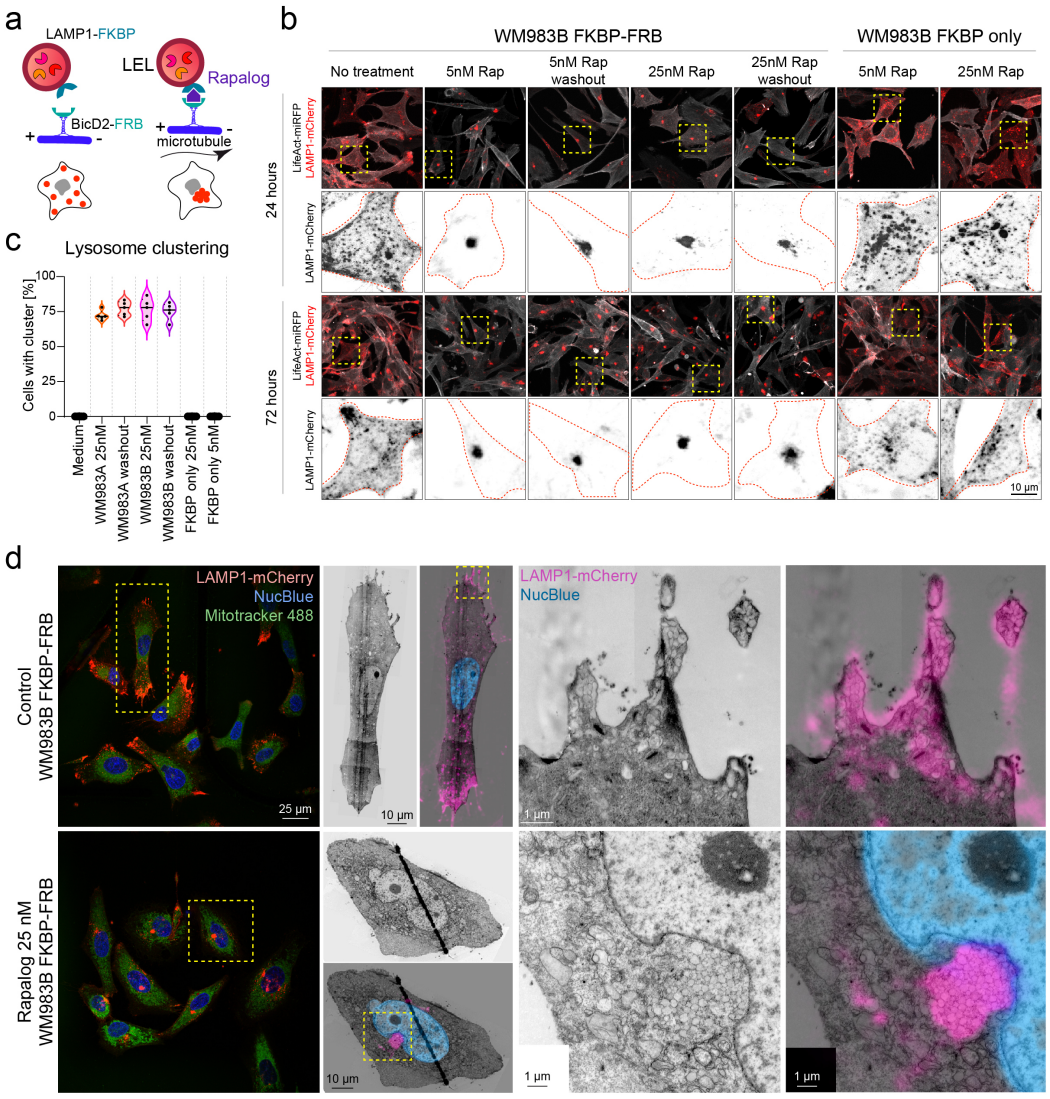

Fig. 2. Induced lysosome clustering in melanoma cells a) Lysosomes in WM983A or WM983B cells stably expressing LAMP1-mCherry-FKBP and BicD2-FRB can be clustered using the compound Rapalog (Rap) which induces FKBP-FRB rapid heterodimerization. b) Cells were seeded in glass-bottom dishes, treated with 5nM or 25nM Rapalog and imaged at 24 hours and 72 hours timepoints. Washout condition – cells were treated for 1 hour with Rapalog, washed 3x in PBS and cultured in normal growth medium. WM983B FKBP-FRB = cells expressing both heterodimerizing domains, lysosomes can cluster. WM983B FKBP only = cells expressing only one heterodimerizing domain, clustering is not achieved. Yellow square delineates the zoomed region shown below; red dotted line shows the cell contour. c) Percentage of cells displaying clustered lysosomes was quantified for each condition at 72 hours timepoint. Percentage = 0.0, 73.3 ± 3.6, 78.5 ± 5.1, 77.7 ± 8.3, 76.4 ± 6.2, 0.0, 0.0 respectively. Data come from five randomly selected fields of view per condition. One dot represents 1 field of view. Kruskal-Wallis with Dunn's multiple comparison post-hoc test, adjusted p-value: WM983A Rap vs. washout, $p > 0.9999$, WM983B Rap vs. washout, $p > 0.9999$. d) Correlative light and electron microscopy. WM983B cells expressing LAMP1-mCherry-FKBP and BicD2-FRB were cultured in control medium, or in medium supplemented with 25 nM Rapalog for one hour and imaged by spinning disc microscope. Samples were processed for electron microscopy and imaged by TEM. Representative images with high magnification of spread or clustered lysosomes and overlay of fluorescent and electron microscopy images (LAMP1 appears in pink, nucleus in blue) are shown for each condition.

arrest in the vasculature after injection (Fig 4b). Melanoma cells with spread lysosomes efficiently extravasated, and displayed high metastatic potential in vivo (Fig 4c, left). On the contrary, when lysosomes were clustered in melanoma cells before injection, their ability to invade from the primary tumor site was strongly impaired (Fig 4c, right) although they had similarly completed intravascular arrest and extravasation as quantified by their post-extravasation invasion potential (Figure 4d, Figure S4a, b). Collectively, these data show that lysosome positioning is an important driver of cell aggressiveness, contributing to the ECM remodeling and to cell invasiveness. As seen in our study, cells with peripheral lysosomes have higher invasion potential in vitro as well as in vivo, which can be rescued by promoting the perinuclear lysosome clustering and thus reducing their malignancy, providing the first in vivo evidence for the role of lysosome positioning in metastatic progression. Organelles are dynamic, self-organized structures whose specific function is inevitably linked to their position and morphology (Schauer et al. 2010), in space and time within cells (Ballabio and Bonifacino, 2020; van Bergeijk et al., 2016). In this study, we provide the first mechanistic demonstration that the position of lysosomes within cells tightly controls the targeted secretion of matrix-degrading enzymes which subse-

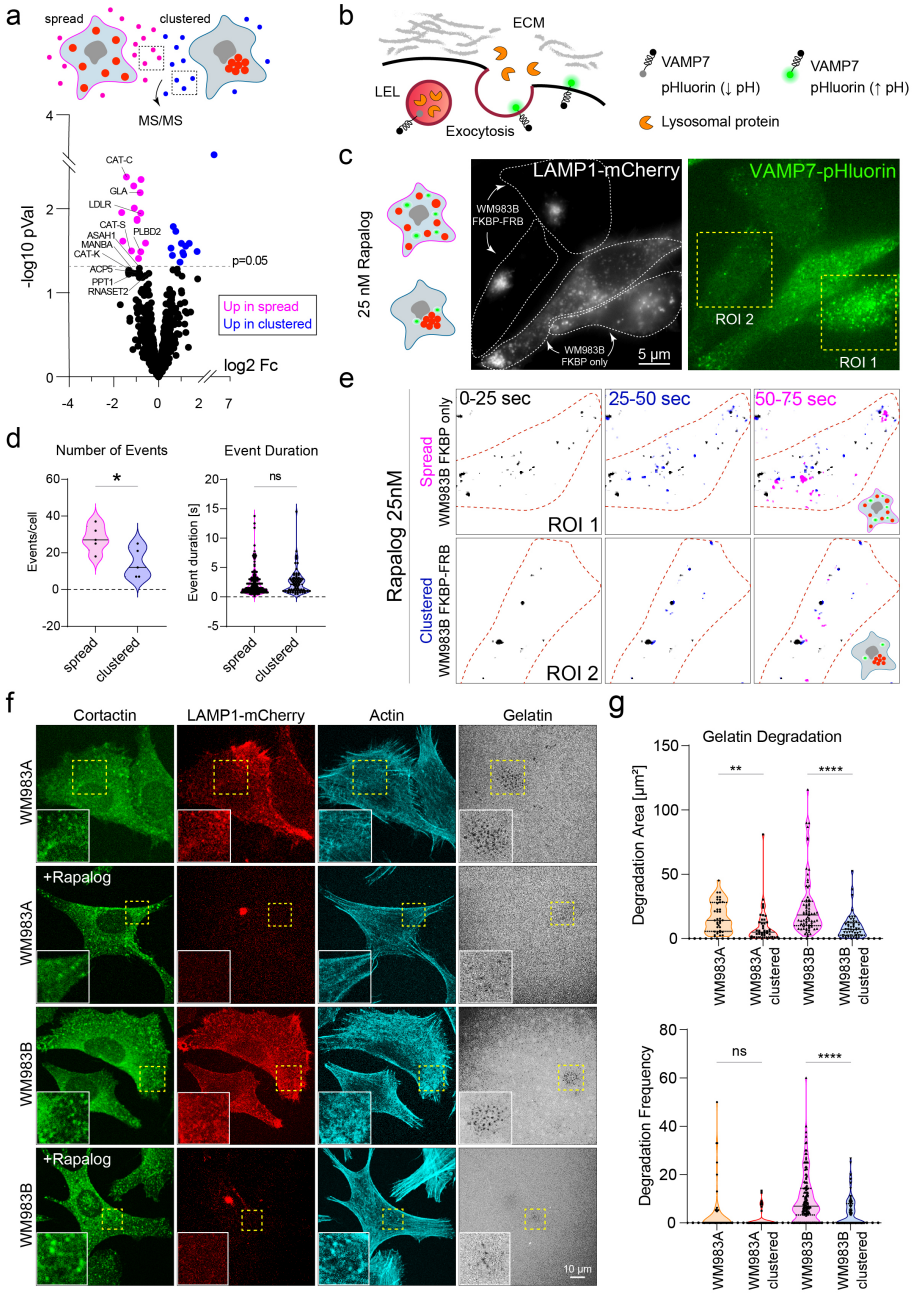

Fig. 3. Lysosome clustering inhibits lysosome secretion and matrix degradation a) Differential quantitative mass spectrometry analysis of proteins secreted in the cell medium by WM983B cells expressing LAMP1-mCherry-FKBP and BicD2-FRB. Cells were cultured in serum-free medium for 24 hours in the absence or presence of 5nM Rapalog. Each dot represents a protein. Proteins known to be lysosome-associated are labelled with their name. Magenta = proteins upregulated in cells with spread lysosomes, blue = proteins upregulated in cells with clustered lysosomes ($p<0,05$). b-e) Lysosome secretion was assessed by TIRF microscopy using VAMP7-pHluorin probe, which is quenched in lysosome acidic environment and has bright fluorescence once exposed to the alkaline pH of the extracellular space. c) WM983B-LAMP1-mCherry cells expressing single heterodimerizing domain (FKBP only) and both the domains (FKBP-FRB) were co-cultured, treated with 25nM Rapalog for 1 hour and analyzed by TIRF microscopy. d) Number of secretion events (left graph, one dot represents one cell) and event duration (right graph, one dot represents one event) were manually counted in five different cells of each type. Events per cell, spread = 27.80 ± 7.19, clustered = 14.40 ± 8.23, p value = 0.0397, Mann-Whitney test. Event duration, spread = 2.46 ± 2.36, clustered = 2.56 ± 2.20 seconds, p value = 0.3518, Mann-Whitney test. e) TIRF movie was divided into three time-segments (black: 0-25 seconds, blue: 25-50 seconds, magenta: 50-75 seconds) and displayed as maximum projection showing the number of events per each time-segment. Two representative examples from panel c are shown, ROI 1 = spread lysosomes, ROI 2 = clustered lysosomes. f-g) WM983A or WM983B cells expressing LAMP1-mCherry-FKBP and BicD2-FRB were cultured on FITC-gelatin in presence or absence of 25nM Rapalog for 24 hours, fixed and stained with cortactin antibody and Phalloidin and imaged by confocal microscopy. g) Degradation area (DA) per cell and degradation frequency (DF) were quantified from the immunofluorescence images. DA (Mean ± SD) = 16.94 ± 11.71 n= 36 cells, 9.38 ± 13.47 n= 45 cells, 24.75 ± 23.29 n= 73 cells, 9.41 ± 9.94 n= 50 cells, respectively, in triplicate. DF (Mean ± SD) = 3.62 ± 9.73 n= 57 cells, 1.49 ± 3.44 n= 58 cells, 10.14 ± 10.45 n= 138 cells, 4.43 ± 6.04 n= 102 cells, respectively, in triplicate, Kruskal-Wallis with Dunn's multiple comparison post-hoc test. One dot represents one cell. *$p<0,05$; ** $p<0,01$; *** $p<0,001$; **** $p<0,0001$.

quently promotes melanoma cell invasion and metastatic progression. This echoes a parallel study showing that relocalization of lysosomes to the cell periphery promotes the emergence of leader cells in collective epithelial cell migration (Marwaha et al., 2023). While more work is required to understand the switches that relocalize lysosomes, both studies demonstrate that peripheral lysosome positioning can impact cell migration, through different mechanisms, either through lysosomal secretion (our study) or through a Rac1-dependent control of actin polymerization and lamellipodium formation (Marwaha et al., 2023). In addition, lysosome repositioning could potentially alter tumor progression by mediating nutrient sensing (Korolchuk et al., 2011) or chemoresistance through the secretion of chemotherapeutics stored in lysosomes (Machado et al., 2015). Probing of spatial distribution and morphology of lysosomes in tumors could constitute a novel indicator of tumor progression, as it is the case for cell shape or additional morphometric analysis (Sero et al., 2015; Pei-Hsun Wu et al., 2020). Several other organelles, such as mitochondria, are intimately linked to cancer progression and probing simultaneously all organelles, as it can be done using whole-cell segmentation of high-resolution images (Heinrich et al., 2021), could document precisely which organelles, and their contacts, are repositioned during melanoma progression. Interestingly, deep learning-based approaches recently demonstrated the power of correlating breast cancer status with organelle topology, which out-performed morphology-based features, further highlighting the need to consider organelles positioning, and their interactome, as a new cancer rheostat that could be exploited for better diagnosis (Wang et al., 2023).

Methods

Antibodies Anti-Cortactin (p80/85) clone 4F11 (ref. n°05-180-I) and Anti-LAMP1 (ref. n°L1418) are from Merck (Sigma-Aldrich). Alexa FluorTM 488 Phalloidin (ref. n° A12379), Alexa FluorTM 568 Phalloidin (ref. n°A12380), Alexa FluorTM 647 Phalloidin (ref. n°A22287) and Alexa Fluor–conjugated secondary antibodies, are all from Thermo Fisher Scientific. Secondary antibodies include Alexa FluorTM 405 conjugated Goat anti-Rabbit (ref. n°A-31556), Alexa FluorTM 488 conjugated Goat anti-Rabbit (ref. n°A-11034), Alexa FluorTM 555 conjugated Goat anti-Rabbit (ref. n°A21429) Alexa FluorTM 647 conjugated Goat anti-Rabbit (ref. n°A-21244).

Cell culture Primary human melanoma cell lines were purchased from Rockland and cultured in MCDB153 (ref. n°M7403, Merck/Sigma-Aldrich) and Leibovitz's L-15 medium (ref. n°11415064, Thermo Fisher Scientific) in a 4 to 1 ratio, supplemented with 2 per cent foetal bovine serum, 1.68 mM CaCl2 and 1 per cent penicillin/streptomycin.

Lentivirus transduction and plasmid transfection Transduction: pLSFFV-LAMP1-mCherry-FKBP (FK506 binding protein), pLSFFV-BicD-FRB (FKBP-rapamycin binding domain) and pLSFFV-LifeActin-miRFP lentivirus were produced in HEK293T cells using JetPRIME® transfection reagent (Polyplus). WM983B cells were infected by lentivirus in the presence of 5µg/mL polybrene (ref. n°TR-1003, Merck/Sigma-Aldrich) followed by antibiotic selection (puromycin 1µg/mL, blasticidin 5µg/mL, hygromycin 200µg/ml). Transfection: Cenexin-GFP plasmid was transfected using JetOPTIMUS® transfection reagent (Polyplus) in a live-video dish, 46h prior experiment.

Invasion assay The 3D collagen invasion assay was adapted from (Sadok et al., 2015). Briefly, melanoma cell lines at 3x105 cells/ml were labelled with Hoechst 33342 and suspended in 3mg/mL of serum free solution of neutralized Type I Bovine Collagen (PureCol® 5005-B, Advanced Biomatrix). Then, 600µL were distributed into black 24 well plates (ref. n°058062, Dutscher) coated with bovine serum albumin. The plates were centrifuged at 1500 rpm at 4°C for 5min and incubated at 37°C for 3 hours. Once collagen had polymerized, medium supplemented with 10 per cent foetal bovine serum, 100ng/mL EGF was added on top of the collagen. 24h after, cells were observed using a Leica TSC SPE confocal microscope (x20 HCX Pl Apo 0.7 NA objective, Wetzlar, Germany) and z-stacks were acquired. Four fields per sample were imaged. Nuclear localization was quantified by IMARIS (interactive microscopy image analysis software) at each plane. The invasion index was calculated by reporting the number of cells above 10µM on the total number of cells by field.

Matrix degradation assay and immunofluorescence Glass coverslips were coated with fluorescent-labelled-FITC gelatine or Cy3 gelatine as described previously (Kolli-Bouhafs et al., 2014). Then, previously starved melanoma cells expressing or not LAMP1-mCherry-FKBP and BicD2-FRB were plated on fluorescent gelatine and incubated at 37°C for 6 to 24h in medium supplemented with 10 per cent foetal bovine serum with or without Rapalog. Cells were fixed using 4 per cent paraformaldehyde permeabilized using triton-X-100 at 0,1 per cent and incubated in 2 per cent of bovine serum albumin at room temperature. Cells were then labelled for 1h with Anti-Cortactin (1/250). After three washes with PBS, cells were incubated with either Alexa FluorTM 405 conjugated Goat anti-Rabbit (1/1000), Alexa FluorTM 488 conjugated Goat anti-Rabbit (1/1000) or Alexa FluorTM 647 conjugated Goat anti-Rabbit (1/1000) and Alexa FluorTM 568 Phalloidin (1/250) or Alexa FluorTM 647 Phalloidin (1/250) for 1h, washed and mounted in ProLongTM Gold Antifade Mountant (ref. n°P10144, Thermo Fisher Scientific). Cells were imaged using Leica TSC SPE or SP8 confocal microscope (x63 HCX Pl Apo 1.40 NA or x20 HCX Pl Apo 0.7 NA objective, Wetzlar, Germany). Invadopodia were identified as actin and cortactin rich punctate structure. Areas of degradation were identified as "black holes" within the fluorescent gelatine. Invadopodia and areas of degradations were quantified using ImageJ software. Degradation areas measurements were based on cells displaying degradation activity, and the frequency of degradation was based on randomly selected cells. Maximum filter, background subtraction and gaussian blur filters were then applied to extract the gel degradation areas by thresholding. Then, M1 Manders coefficients between Lamp1 and inverted Gelatin inten-

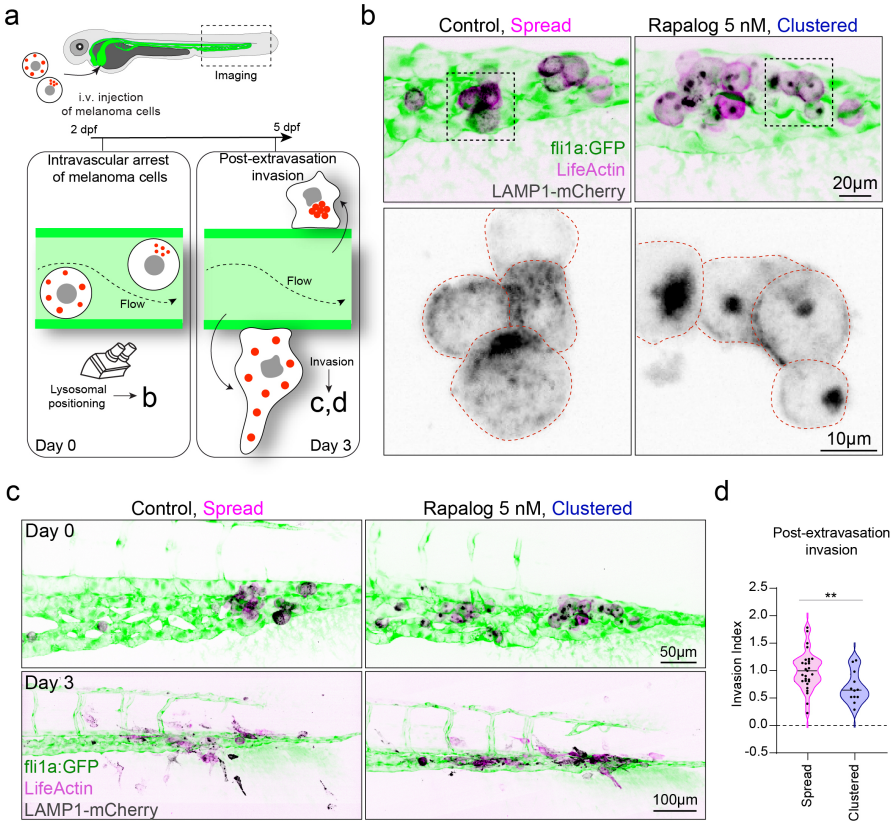

Fig. 4. Lysosome clustering impairs cancer cell invasion in vivo a) Fli1a:GFP (green endothelium) zebrafish embryos (48 hpf) were injected intra-vascularly with WM983B cells having either spread or clustered lysosomes and imaged by confocal microscopy at day 0 and day 3 post injection to assess the post-extravasation invasion potential of cancer cells with different lysosomal positioning. b) WM983B cells stably expressing LAMP1-mCherry-FKBP, BicD2-FRB and LifeActin-miRFP were cultured in medium or in medium supplemented with 5nM Rapalog for 1 hour before injection. Representative confocal images at 3 hours post-injection are shown as maximum z projection for each condition, control = spread lysosomes, 5nM Rapalog = clustered lysosomes. c) Zebrafish embryos were imaged at day 0 (3 hours after cell injection) and at day 3 (72 hours post injection) using a spinning disc microscope. Representative images are shown as a maximum z projection. d) Post-extravasation invasion (PEI) potential was calculated as a proportion of cells (area) that migrated outside of the vasculature region to the total area of cells. PEI (Mean ± SD), control = 1.000 ± 0.3491 n= 29 embryos, clustered = 0.696 ± 0.285 n= 12 embryos, in triplicate, p value = 0.0090, Mann-Whitney test. One dot represents one fish, normalized to control.

sity pictures for these selections were calculated using the colocalization finder plugin.

Clustering dynamics, washout experiments proliferation assay Mechanism of lysosome clustering: clustering was performed by heterodimerization between LAMP1-mCherry-FKBP (lysomes) and BicD-FRB (dynein adaptor) by the use of Rapalog (A/C Heterodimerizer ref. n°635057, from Takara Bio Inc.). Cells were cultured in glass bottom dishes and imaged at different time points (24, 48 and 72 hours) using Olympus Spinning Disk (60X objective, N.A. 1.2). To establish time needed for lysosome clustering, WM983A and WM983B cells expressing both heterodimerizing domains (FKBP-FRB) were treated with 5nM or 25nM Rapalog and followed in time. Time to appearance of lysosome cluster was counted. Washout experiments: WM983B cells expressing either one (FKBP only) or two (FKBP-FRB) heterodimerizing domains were cultured in medium supplemented with 5nM or 25nM Rapalog. To assess the stability of clustering, cells were treated for 1h with 5nM or 25nM Rapalog, washed 3x in PBS and cultured in normal medium for the duration of the experiment. Cells cultured in normal growth medium were used as a control. Proliferation assay: proliferation rates of WM983B cells treated with increasing concentrations of Rapalog were analyzed using the Incucyte® Live-Cell Analysis System. Confluences were automatically calculated by the Incucyte® software based on bright field images, all values are normalized to time zero. Acquisition was performed for 96h.

Micropatterning Immunofluorescence Micropatterns were prepared using photo-lithography methods as previously described (Duong et al., 2012; Schauer et al., 2010). Briefly, cover slides were cleaned in EtOH, dried, cleaned with UV for 10 minutes, coated in PLL-PEG and exposed to UV 10 minutes through a Photomask with 36µm crossbow micropatterns. Coverslips were coated in Fibronectin (40µg/ml – ref. n°F1141 Merck/Sigma-Aldrich). WM1862, WM983A, WM983B cells were trypsinized, resuspended in 5ml culture medium and seeded an micropatterned coverslips. Cells were let to spread for 4 hours before fixing them in 4 per cent PFA. For micropatterning, cells were fixed in 4 per cent PFA, washed 3x in PBS, permeabilized in saponin 0.5 per cent / 2 per cent BSA in PBS for 20 minutes, blocked 30 minutes

in 2 per cent BSA, stained with Anti-LAMP1 (ref. n°L1418) primary antibody for 1 hour, washed 3x in PBS, stained with Alexa FluorTM 555 secondary Goat anti-Rabbit (1:500) and Alexa Fluor™ 488 Phalloidin (1:200) 45 minutes. Mounted in Fluoromount-GTM mounting medium (ref. n°00-4958-02, Thermo Fisher Scientific with DAPI. Z stacks were acquired for the full cell volume (0.2µm between layers) using an Olympus Spinning Disk (60X objective, N.A. 1.2). Image analysis and processing were performed using the Fiji (2.0.0) (Schindelin et al., 2012), Cell Profiler (4.2.1) (Stirling et al., 2021), Metamorph and R software.

Live cell imaging For live cell imaging, Lamp1-mCherry and Lifeact-miRFP expressing cells were plated on fluorescent gelatin-coated coverslips and mounted in a Ludin Chamber (Life Imaging Services). The cells were then placed at 37°C, 5 per cent CO2 on an iMIC microscope equipped with a multi-LED Lumencor Spectra X. Images were acquired with an Olympus 60x TIRFM (1.45 NA) objective every 2.5min during 4h and a Hamamatsu Flash 4 V2+ camera (Iwata) piloted by the Live Aquisition software (Till Photonics). Expressing cells were initially located via both the mCherry and Lifeact-miRFP signals, and were subsequently followed via dual phase contrast/fluorescent signal together with the FITC-coupled gelatin substrate. 10 to 20 different fields were sequentially recorded during each experiment using a Marzhauser Motorized Stage piloted by the iMIC software. JeasyTFM software were then used for automatic selection and repositioning of the best focused images in all channels and time-points. Mean fluorescence intensity of actin, Lamp1 and the underlying substrate at each time points were calculated at invadopodia identified using gelatin degradation.

TIRF microscopy WM983B cells expressing FKBP only (spread) and WM983B cells expressing both FKBP and FRB (clustered) were mixed in an 1:1 ratio, seeded in fibronectin-coated low glass bottom µ-Dish 35mm (ref. n°80137, Ibidi) 48h prior to imaging, treated with 25nM Rapalog for 1h. Imaging was performed in culture medium using an inverted Leica DMI8 microscope (objective 100X HC PL APO 1,47 oil). Recording was done with an Evolve® 512 camera (for TIRF-HILO), at 512X512 pixels resolution, at an acquisition rate of 250ms between frames, for a total duration of 90 seconds, with AFC (Adaptive Focus Control). Exocytosis events were identified based on VAMP7-pHluorin signal, marking lysosome exocytosis (Lachuer et al., 2023). Secretion events were detected and counted manually.

Experimental metastasis assay in zebrafish All zebrafish (ZF) procedures were performed in accordance with French and European Union animal welfare guidelines and supervised by local ethics committee (Animal facility A6748233; APAFIS 2018092515234191). Tg(fli1a:eGFP) (Lawson and Weinstein, 2002) embryos were maintained in Danieau 0.3X medium (17.4mM NaCl, 0.2mM KCl, 0.1mM MgSO4, 0.2mM Ca(NO3)2) buffered with HEPES 0.15mM (pH=7.6), supplemented with 200µM of 1-phenyl-2-thiourea (PTU, ref. n°P7629, Merck/Sigma-Aldrich) to avoid pigmentation. Two days post-fertilization (2dpf) embryos were mounted in 0.8 per cent ultrapure low melting point agarose (Invitrogen) containing 0.17mg/ml tricaine (ethyl-3-aminobenzoate-methanesulfonate, ref. n°E10521, Merck/Sigma-Aldrich). WM983B cells of different lysosome clustering status (spread, clustered) were injected with a Nanoject II Auto-Nanoliter Injector (Drummond Scientific Company) and microforged glass capillaries (25 to 30µm inner diameter) filled with mineral oil (ref. n°M5904, Merck/Sigma-Alrich). 13.8nL of cell suspension from confluent T25 flasks (50x106 cells per ml approx.) were injected in the duct of Cuvier under a M205 FA Fluorescence stereomicroscope (Leica), as previously described (Stoletov et al., 2010). Embryos were injected with WM983B cells or with WM983B cells treated with 5nM rapalog 1h prior to injection, and then kept in Danieau with PTU. Caudal plexus was recorded at day 0 (injection day) and 3dpi using the inverted spinning-disk Olympus IXplore Spin, 30x / 1.05 NA (silicone) objective. Z-stacks of the caudal plexus were acquired for each embryo (3µm or 5µm between layers, at day 0 and 3dpi respectively) with the following settings: 488nm laser at 2 per cent for 100ms / 561nm laser at 15 per cent for 300ms / 640nm laser at 15 per cent for 300ms). Detailed lysosome status (Fig.4b) was imaged at 3 hpi using a 60x/1.2 NA (water) objective.

Correlative Light and Electron Microscopy (CLEM) WM983B cells expressing LAMP1-mCherry-FKBP and BicD2-FRB were cultured in control medium, or in medium supplemented with 25nM Rapalog for one hour and imaged with an Olympus Spinning Disk (60X objective, N.A. 1.2). The samples were then chemically fixed right after the photonic acquisition with 0,05 per cent malachite green, 2.5 per cent glutaraldehyde in 0.1M sodium cacodylate buffer (NaCac), pH7.4 during 30min in an ice bath. Subsequently the samples were post-fixed in 1 per cent OsO4 - 0.8 per cent K3[Fe(CN)6] - 0.1M NaCac buffer pH7.4 (under a fume hood) kept in an ice bath for 50 min, and then washed 2 times with in ice-cold 0.1M NaCac. Then the samples were incubated in 1 per cent aqueous tannic acid solution for 25 min in an ice bath and finally washed 5 times with distilled water. Samples were then kept in 1 per cent uranyl acetate aqueous solution overnight at 4°C sheltered from the light. The samples were serial dehydrated with ethanol solutions (25 per cent, 50 per cent, 70 per cent 95 per cent and 100 per cent). Subsequently the samples were incubated in a serial resin-ethanol 100 per cent mix (1:3; 1:1; 3:1), ending with an incubation in 100 per cent Epon resin 3 times 1h at room temperature. The samples were allowed to polymerize in an oven at 60°C for 48h. The resin blocks were trimmed by ultramicrotomy, 90nm thin sections were collected and placed in copper/formvar slot grids. The transmission electron microscopy (TEM) data sets were acquired with a Hitachi 7500 TEM, with 80 kV beam voltage, and the 8-bit images were obtained with a Hamamatsu camera C4742-51-12NR. Correlative light and electron images were obtained/combined using Adobe Photoshop v.24.4.

Image analysis Organelles segmentation was performed using MetaMorph Microscopy Automation and Image Analysis Software (Molecular Devices) and the ImageJ Modular Image Analysis (MIA) plugin. Segmentation on LAMP1

images were performed to get coordinates for individual LAMP1+ objects and their number. 3D Density maps and inter-organelle distance and distance to barycenter were obtained through the use of R software. Cell invasion in zebrafish was performed by ImageJ Cell Profiler (Molecular Devices) software. Zebrafish images were divided into 6 regions – plexus and 5 regions outside (bins). Area of cells was quantified for each region using Cell Profiler and percentage of cells (from total) was calculated per each region and plotted in a graph. Invasion potential was calculated as area under the curve for all cells that extravasated and invaded outside of the vasculature region.

Mass Spectrometry - Quantitative Proteomics A PierceTM 660nm protein assay quantification (ref. n°22660, Thermo Fisher Scientific), 2µg of each protein extract were digested using the automated Single Pot Solid Phase enhanced Sample Preparation (SP3) protocol as described in (Hughes et al., 2019) on the Bravo AssayMAP platform (Agilent Technologies). Extracted peptides were cleaned-up using automated C18 solid phase extraction on the same platform and analysed by nanoLC-MS/MS on a nanoUPLC system (nanoAcquityUPLC, Waters) coupled to a quadrupole-Orbitrap mass spectrometer (Q-Exactive HF-X, Thermo Scientific). Chromatographic separation was conducted over a 60 minutes linear gradient from 2 to 40 per cent of solvent B (0.1 per cent formic acid in acetonitrile) at a flow rate of 350 nL/min. A Top 10 method was used with automatic switching between MS and MS/MS modes to acquire high resolution MS/MS spectra. To minimize carry-over, a solvent blank injection was performed after each sample. NanoLC-MS/MS data was interpreted to do label-free extracted ion chromatogram-based differential analysis. Searches were done using Mascot software (version 2.5.1, MatrixScience) against a composite database including Homo Sapiens and Bos Taurus protein sequences, which were downloaded from UniProtKB-SwissProt (28-07-2021; 26.031 sequences, Taxonomy ID: 9913 and 9606 respectively) to which common contaminants and decoy sequences were added. One trypsin missed cleavage was tolerated. Carbamidomethylation of cysteine residues was set as a fixed modification. Oxidation of methionine residues and acetylation of proteins n-termini were set as variable modifications. Identification results were imported into the Proline software (version 2.2.0) (Bouyssié et al., 2020) and validated. The maximum false discovery rate was set at 1 per cent at peptide and protein levels with the use of a decoy strategy. Peptides abundances were extracted with cross assignment between all samples. Protein abundances were computed using the best ion of the unique peptide abundances normalized at the peptide level using the median.To be considered, proteins must be identified in at least three out of the four replicates in at least one condition. The imputation of the missing values and differential data analysis were performed using the open-source ProStaR software (version 1.30.7) (Wieczorek et al., 2017). Imputation of missing values was done using the approximation of the lower limit of quantification by the 2.5 per cent lower quantile of each replicate intensity distribution ("det quantile"). A Limma moderated t-test was applied on the dataset to perform differential analysis. The adaptive Benjamini-Hochberg procedure was applied to adjust the p-values and False Discovery Rate. The mass spectrometry proteomics data have been deposited to the ProteomeXchange Consortium via the PRIDE partner repository (Perez-Riverol et al., 2022) with the dataset identifier PXD042007.

Transcriptomic analysis RNA integrity was assessed by Bioanalyzer (total RNA Pico Kit, 2100 Instrument, Agilent Technologies, Paolo Alto, CA, USA). All samples had RNA integrity numbers above 9.5. Sequencing libraries were prepared using "NEBNext Ultra II Directional RNA Library Prep Kit for Illumina" combined with "NEB Ultra II polyA mRNA magnetic isolation" for mRNA enrichment (New England Biolabs, Ipswich, MA, USA). Libraries were pooled and sequenced (single-end, 100bp) on a NextSeq2000 according to the manufacturer's instructions (Illumina Inc., San Diego, CA, USA). For each sample, quality control was carried out and assessed with the NGS Core Tool FastQC (Andrews S, 2010). Sequence reads (minimum 33 Million per sample) were mapped to Homo Sapiens genome version GRCh38 using STAR (Dobin et al., 2013) to obtain a BAM (Binary Alignment Map) file. An abundance matrix was generated based on read counts identified by Featurecounts (Liao et al., 2014) using default parameters. At last, differential expression analyses were performed using the DEseq2 (Love et al., 2014) package of the Bioconductor framework for RNASeq data (Gentleman et al., 2004). Up- and down-regulated genes were selected based on the adjusted p-value (< 0.05) and the fold-change (> 1.5). Functional enrichment analyses were performed using STRING v11 (Szklarczyk et al., 2019) and Gene Ontology (Carbon et a1., 2021). Raw data (FASTQ files) are available at the EMBL-EBI ArrayExpress archive (Accession number E-MTAB-13165).

Statistical analyses Statistical analysis of the results was done using GraphPad Prism 9 (version 9.5.1 for Windows). Mann-Whitney (two groups) or Kruskal-Wallis (>2 groups) statistical tests were performed as specified in the figure legends, to the exception of quantitative proteomics and transcriptomic analysis which have dedicated statistical methodologies specified above. Illustrations of the statistical analyses are displayed in the figures as the mean +/- standard deviation (SD). p-Values smaller than 0.05 were considered as statistically significant. *, p<0.05, **, p<0.01, ***, p<0.001, ****, p<0.0001.

Acknowledgements We thank all members of J.G. Goetz's and K. Schauer teams for discussions on this topic. J.G. Goetz is the coordinator of the NANOTUMOR Consortium, a program from ITMO Cancer of AVIESAN (Alliance Nationale pour les Sciences de la Vie et de la Santé, National Alliance for Life Sciences Health) within the framework of the Cancer Plan (France) that has mostly supported this work, including the teams of KS and PR. Work and people in the lab of J.G. are also supported by the INCa (Insti-

tut National Du Cancer, French National Cancer Institute), charities (La Ligue contre le Cancer, which also supports PR, and ARC (Association pour la Recherche contre le Cancer), FRM (Fondation pour la Recherche Médicale)), the National Plan Cancer initiative, the Region Est, INSERM and the University of Strasbourg. Proteomics experiments were supported by the French Proteomic Infrastructure (ProFI FR2048, ANR-10-INBS-08-03). K. Jerabkova-Roda is supported by a post-doctoral fellowship SPF202004011876 from FRM and the NANOTUMOR consortium. HL was supported by ARC (Association pour la Recherche contre le Cancer) and FRM (Fondation pour la Recherche Médicale). We are also thankful to recent donators (Rohan Athlétisme Saverne) to support our work. The imaging was supported by CRBS imaging platform PIC-STRA with assistance from P. Kessler, by the Imaging Center of IGBMC with assistance from E. Grandgirard and E. Guiot and by the PIQ Platform with assistance from R. Vauchelles.. We acknowledge the Cell and Tissue Imaging Platform (PICT-IBiSA), member of the national infrastructure France-BioImaging supported by the French National Research Agency (ANR-10-INBS-04). We are grateful to T.Galli (IPNP, INSERM U1266, Paris) for sharing the VAMP7-pHLuorin constructs. We thank A-C. Reymann and R. Benoit for sharing their resources, D. Sampaio Goncalves for help with ImageJ macro writing and M. Durik for valuable feedback on the work.

Author Contributions KJR, VH, KS, PR and JGG conceived project and designed the experiments. KJR performed most of the experiments and analysis. AM, RK, HJ, LML, PC, ES and PR performed collagen gel invasion assays and invadopodia experiments. KJR, NA and MP performed zebrafish experiments. KJR and IB performed CLEM experiments. AL and OL performed molecular biology. KJR performed and analyzed (with help from HL) micropatterning experiments. AP, TS, AM and RC performed and analyzed RNAseq experiments. AH, FD and CC performed and analyzed mass spectrometry experiments. VH, KS, PR and JGG provided funding. VH and JGG supervised the study. KS and PR co-supervised the study. KJR, VH and JGG wrote the manuscript, with input from KS and PR. All authors proofread the manuscript.

Bibliography

Andrews S, 2010. FastQC: a quality control tool for high throughput sequence data.

Augoff, K., Hryniewicz-Jankowska, A., Tabola, R., 2020. Invadopodia: clearing the way for cancer cell invasion. Ann. Transl. Med. 8, 902. https://doi.org/10.21037/atm.2020.02.157

Ballabio, A., Bonifacino, J.S., 2020. Lysosomes as dynamic regulators of cell and organismal homeostasis. Nat. Rev. Mol. Cell Biol. 21, 101–118. https://doi.org/10.1038/s41580-019-0185-4

Bian, B., Mongrain, S., Cagnol, S., Langlois, M.-J., Boulanger, J., Bernatchez, G., Carrier, J.C., Boudreau, F., Rivard, N., 2016. Cathepsin B promotes colorectal tumorigenesis, cell invasion, and metastasis. Mol. Carcinog. 55, 671–687. https://doi.org/10.1002/mc.22312

Bouyssié, D., Hesse, A.-M., Mouton-Barbosa, E., Rompais, M., Macron, C., Carapito, C., Gonzalez de Peredo, A., Couté, Y., Dupierris, V., Burel, A., Menetrey, J.-P., Kalaitzakis, A., Poisat, J., Romdhani, A., Burlet-Schiltz, O., Cianférani, S., Garin, J., Bruley, C., 2020. Proline: an efficient and user-friendly software suite for large-scale proteomics. Bioinformatics 36, 3148–3155. https://doi.org/10.1093/bioinformatics/btaa118

Braeuer, R.R., Zigler, M., Villares, G.J., Dobroff, A.S., Bar-Eli, M., 2011. Transcriptional Control of Melanoma Metastasis: The Importance of the Tumor Microenvironment. Semin. Cancer Biol. 21, 83–88. https://doi.org/10.1016/j.semcancer.2010.12.007

Chaineau, M., Danglot, L., Galli, T., 2009. Multiple roles of the vesicular-SNARE TI-VAMP in post-Golgi and endosomal trafficking. FEBS Lett. 583, 3817–3826. https://doi.org/10.1016/j.febslet.2009.10.026

Chen, C.-S., Chen, W.-N.U., Zhou, M., Arttamangkul, S., Haugland, R.P., 2000. Probing the cathepsin D using a BODIPY FL–pepstatin A: applications in fluorescence polarization and microscopy. J. Biochem. Biophys. Methods 42, 137–151. https://doi.org/10.1016/S0165-022X(00)00048-8

Circu, M.L., Dykes, S.S., Carroll, J., Kelly, K., Galiano, F., Greer, A., Cardelli, J., El-Osta, H., 2016. A Novel High Content Imaging-Based Screen Identifies the Anti-Helminthic Niclosamide as an Inhibitor of Lysosome Anterograde Trafficking and Prostate Cancer Cell Invasion. PLOS ONE 11, e0146931. https://doi.org/10.1371/journal.pone.0146931

Corrotte, M., Castro-Gomes, T., 2019. Chapter One - Lysosomes and plasma membrane repair, in: Andrade, L.O. (Ed.), Current Topics in Membranes, Plasma Membrane Repair. Academic Press, pp. 1–16. https://doi.org/10.1016/bs.ctm.2019.08.001

da Costa, A.C., Santa-Cruz, F., Mattos, L.A.R., Rêgo Aquino, M.A., Martins, C.R., Bandeira Ferraz, Á.A., Figueiredo, J.L., 2020. Cathepsin S as a target in gastric cancer. Mol. Clin. Oncol. 12, 99–103. https://doi.org/10.3892/mco.2019.1958

Dillekås, H., Rogers, M.S., Straume, O., 2019. Are 90 per cent of deaths from cancer caused by metastases? Cancer Med. 8, 5574–5576. https://doi.org/10.1002/cam4.2474

Dobin, A., Davis, C.A., Schlesinger, F., Drenkow, J., Zaleski, C., Jha, S., Batut, P., Chaisson, M., Gingeras, T.R., 2013. STAR: ultrafast universal RNA-seq aligner. Bioinformatics 29, 15–21. https://doi.org/10.1093/bioinformatics/bts635

Duong, T., Goud, B., Schauer, K., 2012. Closed-form density-based framework for automatic detection of cellular morphology changes. Proc. Natl. Acad. Sci. 109, 8382–8387. https://doi.org/10.1073/pnas.1117796109

Follain, G., Osmani, N., Azevedo, A.S., Allio, G., Mercier, L., Karreman, M.A., Solecki, G., Garcia Leòn, M.J., Lefebvre, O., Fekonja, N., Hille, C., Chabannes, V., Dollé, G., Metivet, T., Hovsepian, F.D., Prudhomme, C., Pichot, A.,

Paul, N., Carapito, R., Bahram, S., Ruthensteiner, B., Kemmling, A., Siemonsen, S., Schneider, T., Fiehler, J., Glatzel, M., Winkler, F., Schwab, Y., Pantel, K., Harlepp, S., Goetz, J.G., 2018. Hemodynamic Forces Tune the Arrest, Adhesion, and Extravasation of Circulating Tumor Cells. Dev. Cell 45, 33-52.e12. https://doi.org/10.1016/j.devcel.2018.02.015

Gentleman, R.C., Carey, V.J., Bates, D.M., Bolstad, B., Dettling, M., Dudoit, S., Ellis, B., Gautier, L., Ge, Y., Gentry, J., Hornik, K., Hothorn, T., Huber, W., Iacus, S., Irizarry, R., Leisch, F., Li, C., Maechler, M., Rossini, A.J., Sawitzki, G., Smith, C., Smyth, G., Tierney, L., Yang, J.Y., Zhang, J., 2004. Bioconductor: open software development for computational biology and bioinformatics. Genome Biol. 5, R80. https://doi.org/10.1186/gb-2004-5-10-r80

Ghoroghi, S., Mary, B., Larnicol, A., Asokan, N., Klein, A., Osmani, N., Busnelli, I., Delalande, F., Paul, N., Halary, S., Gros, F., Fouillen, L., Haeberle, A.-M., Royer, C., Spiegelhalter, C., André-Grégoire, G., Mittelheisser, V., Detappe, A., Murphy, K., Timpson, P., Carapito, R., Blot-Chabaud, M., Gavard, J., Carapito, C., Vitale, N., Lefebvre, O., Goetz, J.G., Hyenne, V., 2021. Ral GTPases promote breast cancer metastasis by controlling biogenesis and organ targeting of exosomes. eLife 10, e61539. https://doi.org/10.7554/eLife.61539

Glunde, K., Guggino, S.E., Solaiyappan, M., Pathak, A.P., Ichikawa, Y., Bhujwalla, Z.M., 2003. Extracellular Acidification Alters Lysosomal Trafficking in Human Breast Cancer Cells. Neoplasia 5, 533–545. https://doi.org/10.1016/S1476-5586(03)80037-4

Heinrich, L., Bennett, D., Ackerman, D., Park, W., Bogovic, J., Eckstein, N., Petruncio, A., Clements, J., Pang, S., Xu, C.S., Funke, J., Korff, W., Hess, H.F., Lippincott-Schwartz, J., Saalfeld, S., Weigel, A.V., 2021. Whole-cell organelle segmentation in volume electron microscopy. Nature 599, 141–146. https://doi.org/10.1038/s41586-021-03977-3

Hoshino, D., Kirkbride, K.C., Costello, K., Clark, E.S., Sinha, S., Grega-Larson, N., Tyska, M.J., Weaver, A.M., 2013. Exosome secretion is enhanced by invadopodia and drives invasive behavior. Cell Rep. 5, 10.1016/j.celrep.2013.10.050. https://doi.org/10.1016/j.celrep.2013.10.050

Hua, H., Li, M., Luo, T., Yin, Y., Jiang, Y., 2011. Matrix metalloproteinases in tumorigenesis: an evolving paradigm. Cell. Mol. Life Sci. CMLS 68, 3853–3868. https://doi.org/10.1007/s00018-011-0763-x

Hughes, C.S., Moggridge, S., Müller, T., Sorensen, P.H., Morin, G.B., Krijgsveld, J., 2019. Single-pot, solid-phase-enhanced sample preparation for proteomics experiments. Nat. Protoc. 14, 68–85. https://doi.org/10.1038/s41596-018-0082-x

Jacob, A., Prekeris, R., 2015. The regulation of MMP targeting to invadopodia during cancer metastasis. Front. Cell Dev. Biol. 3, 4. https://doi.org/10.3389/fcell.2015.00004

Jia, R., Bonifacino, J.S., 2019. Lysosome Positioning Influences mTORC2 and AKT Signaling. Mol. Cell 75, 26-38.e3. https://doi.org/10.1016/j.molcel.2019.05.009

Johnson, D.E., Ostrowski, P., Jaumouillé, V., Grinstein, S., 2016. The position of lysosomes within the cell determines their luminal pH. J. Cell Biol. 212, 677–692. https://doi.org/10.1083/jcb.201507112

Kalluri, R., 2016. The biology and function of fibroblasts in cancer. Nat. Rev. Cancer 16, 582–598. https://doi.org/10.1038/nrc.2016.73

Kapitein, L.C., Schlager, M.A., van der Zwan, W.A., Wulf, P.S., Keijzer, N., Hoogenraad, C.C., 2010. Probing Intracellular Motor Protein Activity Using an Inducible Cargo Trafficking Assay. Biophys. J. 99, 2143–2152. https://doi.org/10.1016/j.bpj.2010.07.055

Kolli-Bouhafs, K., Sick, E., Noulet, F., Gies, J.-P., De Mey, J., Rondé, P., 2014. FAK competes for Src to promote migration against invasion in melanoma cells. Cell Death Dis. 5, e1379. https://doi.org/10.1038/cddis.2014.329

Korolchuk, V.I., Saiki, S., Lichtenberg, M., Siddiqi, F.H., Roberts, E.A., Imarisio, S., Jahreiss, L., Sarkar, S., Futter, M., Menzies, F.M., O'Kane, C.J., Deretic, V., Rubinsztein, D.C., 2011. Lysosomal positioning coordinates cellular nutrient responses. Nat. Cell Biol. 13, 453–460. https://doi.org/10.1038/ncb2204

Lachuer, H., Le, L., Lévêque-Fort, S., Goud, B., Schauer, K., 2023. Spatial organization of lysosomal exocytosis relies on membrane tension gradients. Proc. Natl. Acad. Sci. 120, e2207425120. https://doi.org/10.1073/pnas.2207425120

Lawson, N.D., Weinstein, B.M., 2002. In vivo imaging of embryonic vascular development using transgenic zebrafish. Dev. Biol. 248, 307–318. https://doi.org/10.1006/dbio.2002.0711

Liao, Y., Smyth, G.K., Shi, W., 2014. featureCounts: an efficient general purpose program for assigning sequence reads to genomic features. Bioinformatics 30, 923–930. https://doi.org/10.1093/bioinformatics/btt656

Love, M.I., Huber, W., Anders, S., 2014. Moderated estimation of fold change and dispersion for RNA-seq data with DESeq2. Genome Biol. 15, 550. https://doi.org/10.1186/s13059-014-0550-8

Machado, E., White-Gilbertson, S., van de Vlekkert, D., Janke, L., Moshiach, S., Campos, Y., Finkelstein, D., Gomero, E., Mosca, R., Qiu, X., Morton, C.L., Annunziata, I., d'Azzo, A., 2015. Regulated lysosomal exocytosis mediates cancer progression. Sci. Adv. 1, e1500603. https://doi.org/10.1126/sciadv.1500603

Marwaha, R., Rawal, S., Khuntia, P., Banerjee, S., Manoj, D., Jaiswal, M., Das, T., 2023. Mechanosensitive dynamics of lysosomes along microtubules regulate leader cell emergence in collective cell migration. https://doi.org/10.1101/2022.08.03.502740

Mathur, P., De Barros Santos, C., Lachuer, H., Patat, J., Latgé, B., Radvanyi, F., Goud, B., Schauer, K., 2023. Transcription factor EB regulates phosphatidylinositol-3-phosphate levels that control lysosome positioning in the bladder cancer model. Commun. Biol. 6, 1–14. https://doi.org/10.1038/s42003-023-04501-1

Medina, D.L., Fraldi, A., Bouche, V., Annunziata, F., Mansueto, G., Spampanato, C., Puri, C., Pignata, A., Martina, J.A., Sardiello, M., Palmieri, M., Polishchuk, R., Puertollano,

R., Ballabio, A., 2011. Transcriptional Activation of Lysosomal Exocytosis Promotes Cellular Clearance. Dev. Cell 21, 421–430. https://doi.org/10.1016/j.devcel.2011.07.016

Moamer, A., Hachim, I.Y., Binothman, N., Wang, N., Lebrun, J.-J., Ali, S., 2019. A role for kinesin-1 subunits KIF5B/KLC1 in regulating epithelial mesenchymal plasticity in breast tumorigenesis. EBioMedicine 45, 92–107. https://doi.org/10.1016/j.ebiom.2019.06.009

Monteiro, P., Rossé, C., Castro-Castro, A., Irondelle, M., Lagoutte, E., Paul-Gilloteaux, P., Desnos, C., Formstecher, E., Darchen, F., Perrais, D., Gautreau, A., Hertzog, M., Chavrier, P., 2013. Endosomal WASH and exocyst complexes control exocytosis of MT1-MMP at invadopodia. J. Cell Biol. 203, 1063–1079. https://doi.org/10.1083/jcb.201306162

Mousson, A., Legrand, M., Steffan, T., Vauchelles, R., Carl, P., Gies, J.-P., Lehmann, M., Zuber, G., De Mey, J., Dujardin, D., Sick, E., Rondé, P., 2021. Inhibiting FAK–Paxillin Interaction Reduces Migration and Invadopodia-Mediated Matrix Degradation in Metastatic Melanoma Cells. Cancers 13, 1871. https://doi.org/10.3390/cancers13081871

Naegeli, K.M., Hastie, E., Garde, A., Wang, Z., Keeley, D.P., Gordon, K.L., Pani, A.M., Kelley, L.C., Morrissey, M.A., Chi, Q., Goldstein, B., Sherwood, D.R., 2017. Cell invasion in vivo via rapid exocytosis of a transient lysosome-derived membrane domain. Dev. Cell 43, 403-417.e10. https://doi.org/10.1016/j.devcel.2017.10.024

Nair, S.V., Narendradev, N.D., Nambiar, R.P., Kumar, R., Srinivasula, S.M., 2020. Naturally occurring and tumor-associated variants of RNF167 promote lysosomal exocytosis and plasma membrane resealing. J. Cell Sci. 133, jcs239335. https://doi.org/10.1242/jcs.239335

Perera, R.M., Stoykova, S., Nicolay, B.N., Ross, K.N., Fitamant, J., Boukhali, M., Lengrand, J., Deshpande, V., Selig, M.K., Ferrone, C.R., Settleman, J., Stephanopoulos, G., Dyson, N.J., Zoncu, R., Ramaswamy, S., Haas, W., Bardeesy, N., 2015. Transcriptional control of autophagy–lysosome function drives pancreatic cancer metabolism. Nature 524, 361–365. https://doi.org/10.1038/nature14587

Perez-Riverol, Y., Bai, J., Bandla, C., García-Seisdedos, D., Hewapathirana, S., Kamatchinathan, S., Kundu, D.J., Prakash, A., Frericks-Zipper, A., Eisenacher, M., Walzer, M., Wang, S., Brazma, A., Vizcaíno, J.A., 2022. The PRIDE database resources in 2022: a hub for mass spectrometry-based proteomics evidences. Nucleic Acids Res. 50, D543–D552. https://doi.org/10.1093/nar/gkab1038

Pu, J., Guardia, C.M., Keren-Kaplan, T., Bonifacino, J.S., 2016. Mechanisms and functions of lysosome positioning. J. Cell Sci. 129, 4329–4339. https://doi.org/10.1242/jcs.196287

Sadok, A., McCarthy, A., Caldwell, J., Collins, I., Garrett, M.D., Yeo, M., Hooper, S., Sahai, E., Kuemper, S., Mardakheh, F.K., Marshall, C.J., 2015. Rho Kinase Inhibitors Block Melanoma Cell Migration and Inhibit Metastasis. Cancer Res. 75, 2272–2284. https://doi.org/10.1158/0008-5472.CAN-14-2156

Sahai, E., Astsaturov, I., Cukierman, E., DeNardo, D.G., Egeblad, M., Evans, R.M., Fearon, D., Greten, F.R., Hingorani, S.R., Hunter, T., Hynes, R.O., Jain, R.K., Janowitz, T., Jorgensen, C., Kimmelman, A.C., Kolonin, M.G., Maki, R.G., Powers, R.S., Puré, E., Ramirez, D.C., Scherz-Shouval, R., Sherman, M.H., Stewart, S., Tlsty, T.D., Tuveson, D.A., Watt, F.M., Weaver, V., Weeraratna, A.T., Werb, Z., 2020. A framework for advancing our understanding of cancer-associated fibroblasts. Nat. Rev. Cancer 20, 174–186. https://doi.org/10.1038/s41568-019-0238-1

Schauer, K., Duong, T., Bleakley, K., Bardin, S., Bornens, M., Goud, B., 2010. Probabilistic density maps to study global endomembrane organization. Nat. Methods 7, 560–566. https://doi.org/10.1038/nmeth.1462

Schindelin, J., Arganda-Carreras, I., Frise, E., Kaynig, V., Longair, M., Pietzsch, T., Preibisch, S., Rueden, C., Saalfeld, S., Schmid, B., Tinevez, J.-Y., White, D.J., Hartenstein, V., Eliceiri, K., Tomancak, P., Cardona, A., 2012. Fiji: an open-source platform for biological-image analysis. Nat. Methods 9, 676–682. https://doi.org/10.1038/nmeth.2019

Sero, J.E., Sailem, H.Z., Ardy, R.C., Almuttaqi, H., Zhang, T., Bakal, C., 2015. Cell shape and the microenvironment regulate nuclear translocation of NF-κB in breast epithelial and tumor cells. Mol. Syst. Biol. 11, 790. https://doi.org/10.15252/msb.20145644

Steffan, J.J., Snider, J.L., Skalli, O., Welbourne, T., Cardelli, J.A., 2009. Na+/H+ exchangers and RhoA regulate acidic extracellular pH-induced lysosome trafficking in prostate cancer cells. Traffic Cph. Den. 10, 737–753. https://doi.org/10.1111/j.1600-0854.2009.00904.x

Stirling, D.R., Swain-Bowden, M.J., Lucas, A.M., Carpenter, A.E., Cimini, B.A., Goodman, A., 2021. CellProfiler 4: improvements in speed, utility and usability. BMC Bioinformatics 22, 433. https://doi.org/10.1186/s12859-021-04344-9

Stoletov, K., Kato, H., Zardouzian, E., Kelber, J., Yang, J., Shattil, S., Klemke, R., 2010. Visualizing extravasation dynamics of metastatic tumor cells. J. Cell Sci. 123, 2332–2341. https://doi.org/10.1242/jcs.069443

Tu, C., Ortega-Cava, C.F., Chen, G., Fernandes, N.D., Cavallo-Medved, D., Sloane, B.F., Band, V., Band, H., 2008. Lysosomal cathepsin B participates in the podosome-mediated extracellular matrix degradation and invasion via secreted lysosomes in v-Src fibroblasts. Cancer Res. 68, 9147–9156. https://doi.org/10.1158/0008-5472.CAN-07-5127

van Bergeijk, P., Hoogenraad, C.C., Kapitein, L.C., 2016. Right Time, Right Place: Probing the Functions of Organelle Positioning. Trends Cell Biol. 26, 121–134. https://doi.org/10.1016/j.tcb.2015.10.001

Vidak, E., Javoršek, U., Vizovišek, M., Turk, B., 2019. Cysteine Cathepsins and Their Extracellular Roles: Shaping the Microenvironment. Cells 8, 264. https://doi.org/10.3390/cells8030264

Wang, L., Goldwag, J., Bouyea, M., Barra, J., Matteson, K., Maharjan, N., Eladdadi, A., Embrechts, M.J., Intes, X., Kruger, U., Barroso, M., 2023. Spatial topology of organelle is a new breast cancer cell classifier. iScience 107229. https://doi.org/10.1016/j.isci.2023.107229

Wang, Q., Yao, J., Jin, Q., Wang, X., Zhu, H., Huang, F., Wang, W., Qiang, J., Ni, Q., 2017. LAMP1 expression is associated with poor prognosis in breast cancer. Oncol. Lett. 14, 4729–4735. https://doi.org/10.3892/ol.2017.6757

Weidmann, M.D., Surve, C.R., Eddy, R.J., Chen, X., Gertler, F.B., Sharma, V.P., Condeelis, J.S., 2016. MenaINV dysregulates cortactin phosphorylation to promote invadopodium maturation. Sci. Rep. 6, 36142. https://doi.org/10.1038/srep36142

Wieczorek, S., Combes, F., Lazar, C., Giai Gianetto, Q., Gatto, L., Dorffer, A., Hesse, A.-M., Couté, Y., Ferro, M., Bruley, C., Burger, T., 2017. DAPAR ProStaR: software to perform statistical analyses in quantitative discovery proteomics. Bioinformatics 33, 135–136. https://doi.org/10.1093/bioinformatics/btw580

Winkler, J., Abisoye-Ogunniyan, A., Metcalf, K.J., Werb, Z., 2020. Concepts of extracellular matrix remodelling in tumour progression and metastasis. Nat. Commun. 11, 5120. https://doi.org/10.1038/s41467-020-18794-x

Wu, Pei-Hsun, Gilkes, D.M., Phillip, J.M., Narkar, A., Cheng, T.W.-T., Marchand, J., Lee, M.-H., Li, R., Wirtz, D., 2020. Single-cell morphology encodes metastatic potential. Sci. Adv. 6, eaaw6938. https://doi.org/10.1126/sciadv.aaw6938

Wu, Ping-Hsiu, Onodera, Y., Giaccia, A.J., Le, Q.-T., Shimizu, S., Shirato, H., Nam, J.-M., 2020. Lysosomal trafficking mediated by Arl8b and BORC promotes invasion of cancer cells that survive radiation. Commun. Biol. 3, 620. https://doi.org/10.1038/s42003-020-01339-9

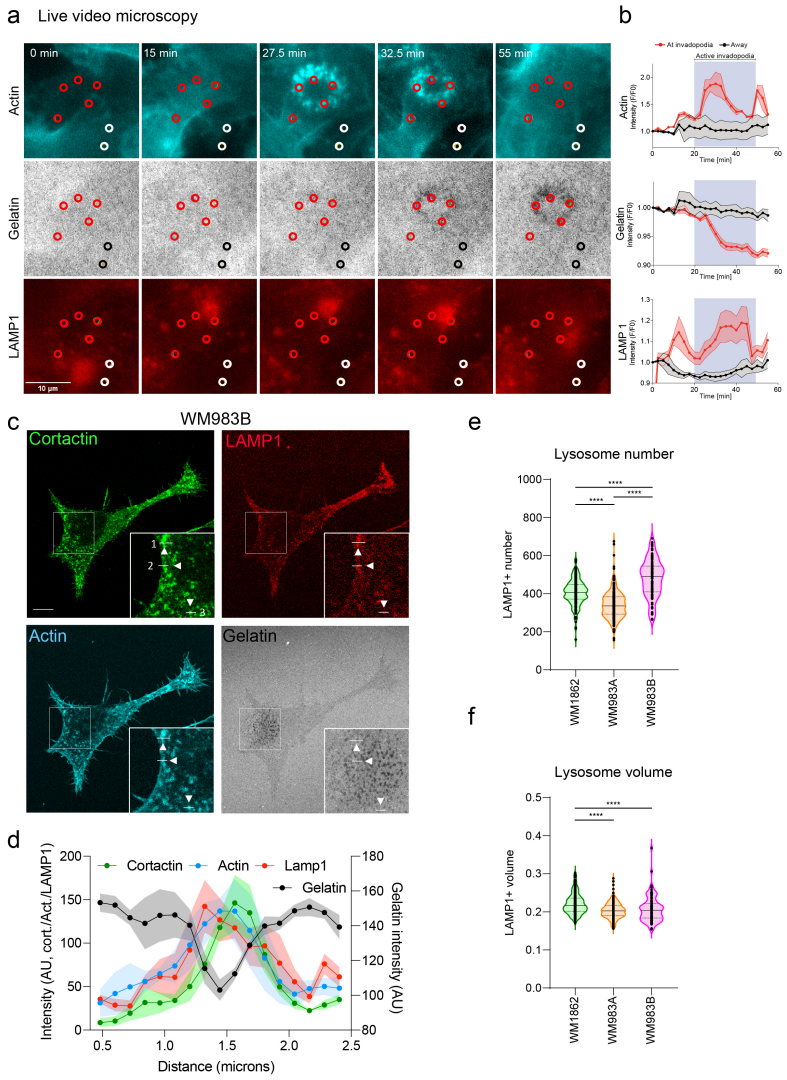

Fig. S1. Lysosomal marker LAMP1 colocalizes with active invadopodia a) WM983B cells stably expressing lysosome marker LAMP1-mCherry and LifeActin-miRFP were seeded on gelatin 24 hours prior to the experiment. Time-lapse movies were acquired during one hour and the signal intensity was quantified in five invadopodia-rich regions (red) and in two regions outside of active invadopodia (gray), blue rectangle marks the duration of active invadopodia. b) Intensity profiles over time are plotted for actin (invadopodia), gelatin (degradation) and LAMP1 (lysosomes). c) WM983B cells were seeded on gelatin 24 hours prior to the experiment, fixed and stained with cortactin, and LAMP1 antibody and with phalloidin (actin). d)The level of colocalization was quantified by line profiling in ImageJ. e-f) Cells were grown on crossbow micropatterns for 4 hours, fixed and stained with LAMP1 antibody. Images were segmented in Metamorph. R software was used to quantify total lysosome number per cell and the average volume of lysosome per cell. One dot represents 1 cell. Kruskal-Wallis with Dunn's multiple comparison post-hoc test. WM1862, n= 182 cells, WM983A, n= 231 cells, WM983B, n= 82 cells, in triplicate. e) Lysosome number (Mean ± SD) = 405.9 ± 68, 341.9 ± 74, 479.7 ± 99, respectively. f) Lysosome volume = 0.2211 ± 0.023, 0.2035 ± 0.021, 0.2071 ± 0.034, respectively. *p<0,05; ** p<0,01; *** p<0,001; **** p<0,0001.

Supplementary material Table 1: Lysosome genes differentially expressed (refers to Fig1g)
Table 2: Postitive Regulation of cell migration genes differentially expressed (refers to Fig1g)

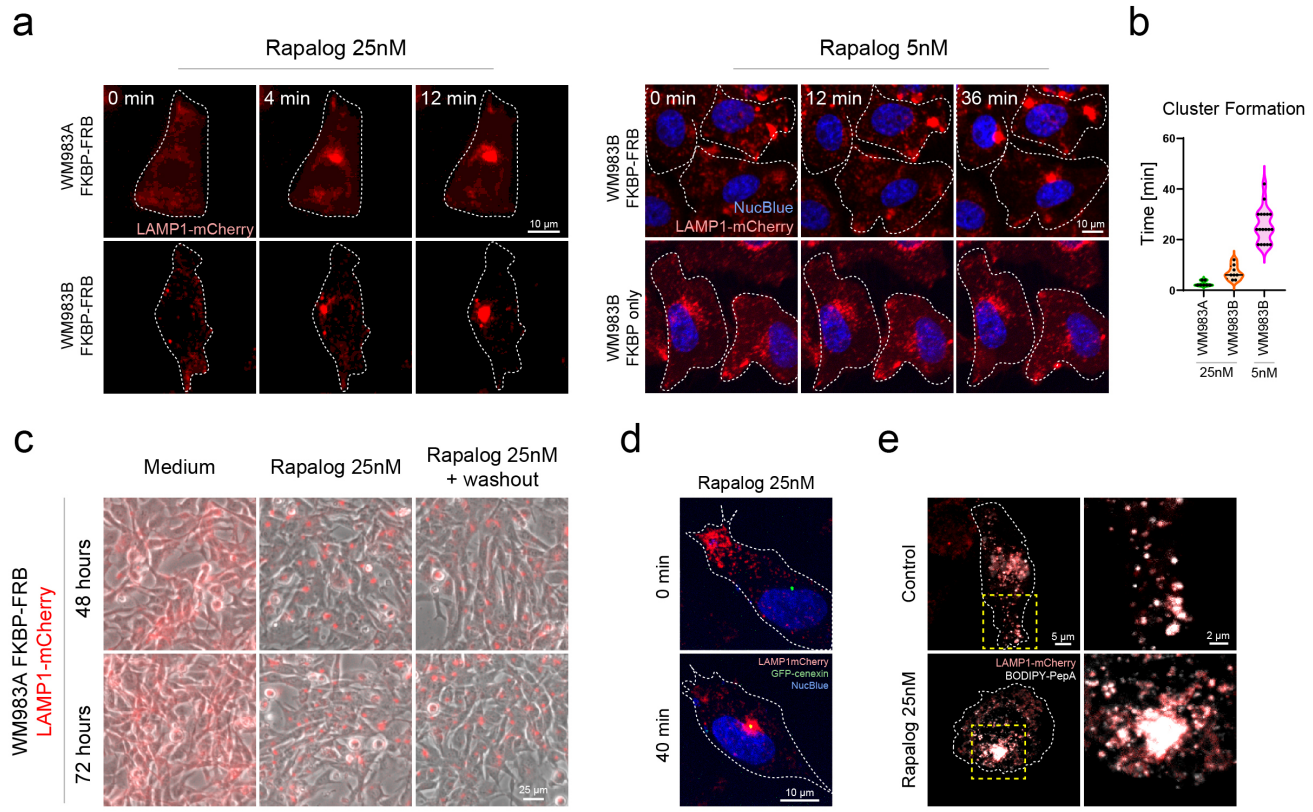

Fig. S2. Dynamics of Rapalog-induced lysosome clustering a) WM983A and WM983B cells expressing two heterodimerizing domains (FKBP-FRB) and WM983B cells expressing only one heterodimerizing domain (FKBP only) were seeded in glass bottom dishes and 1-hour time-lapse movies were acquired using spinning disc. After acquiring the first time-frame, cells were treated with 25 nM Rapalog (left) or with 5 nM Rapalog (right). b) Cluster formation was quantified as the time needed until a visible cluster appeared. Time [min] = 2.6 ± 1.0, 7.0 ± 2.8, 25.7 ± 6.8, respectively. One dot represents 1 cell. c) WM983A (FKBP-FRB) cells were treated with 25 nM Rapalog and imaged at 48 hours and 72 hours timepoints. Washout condition – cells were treated for 1 hour with Rapalog, washed 3x in PBS and cultured in normal growth medium for the duration of the experiment. d) WM983B (FKBP-FRB) cells were seeded in glass bottom dishes and 45 minutes time-lapse movies were acquired using spinning disc. Rapalog induces lysosome clustering around the microtubule organizing center, labelled by cenexin-GFP. e) WM983B (FKBP-FRB) cells expressing LAMP1-mCherry (red) were cultured in medium or in medium with 25 nM Rapalog for 1 hour and then treated with PepstatinA-BODIPY (white) probe for 45 minutes. Cells were imaged live using spinning disc.

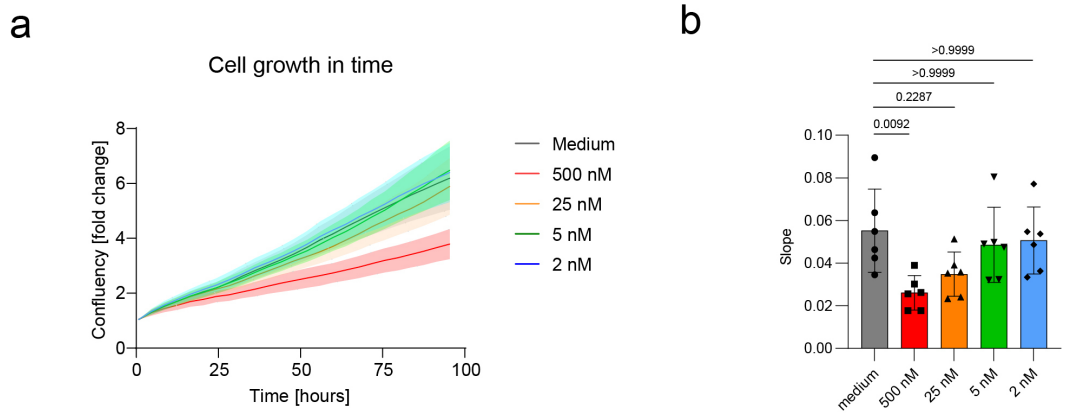

Fig. S3. Low dose of Rapalog treatment does not inhibit cell proliferation a-b) Proliferation rate of WM983B cells treated with increasing concentrations of Rapalog was analyzed using incucyte. a) Cell confluency was quantified for each time-point, all values were normalized to time 0 and the growth curves were plotted. Colored lines depict different culture conditions: medium (black), 2 nM (blue), 5 nM (green), 25 nM (orange), 500 nM Rapalog (red) and are representing average value of three experiments ± SD. b) Slopes were calculated for the different growth conditions. Slope (Mean ± SD) = 0.0552 ± 0.02, 0.0261 ± 0.01, 0.0348 ± 0.01, 0.0486 ± 0.02, 0.0507 ± 0.02, respectively. Kruskal-Wallis test with Dunn's multiple comparison post-hoc test, respective adjusted p-values are shown in the graph. One dot represents one experiment (performed in technical triplicate).

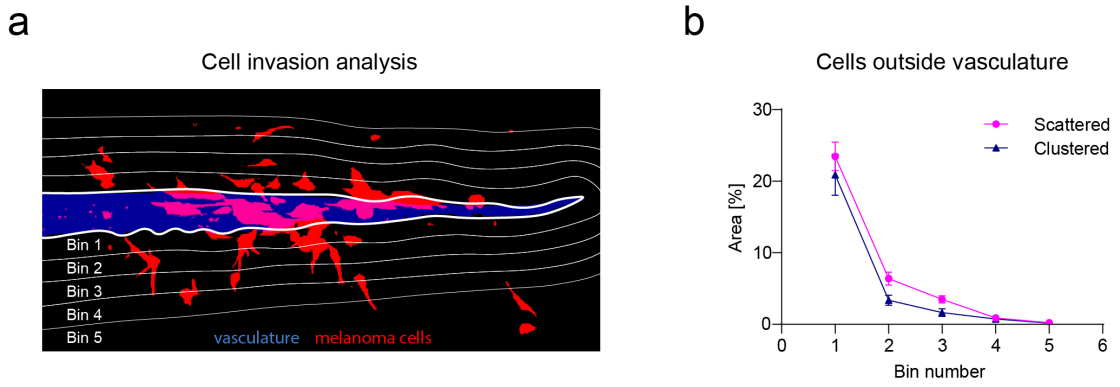

Fig. S4. Monitoring cell invasion in vivo a-b) Quantification of the post-extravasation invasion potential at 72 hours post injection. a) Representative example of the segmented image. Vasculature (blue) and WM983B melanoma cells (red) were segmented using ImageJ. Segmented images were further analyzed using CellProfiler: Image was divided into five regions (bins) with increasing distance from the vasculature region and the total cell are in each region was quantified. b) Percentage of cells (measured from their area) present in each bin was calculated and plotted for both conditions. Magenta = cells with spread lysosomes, blue= cells with clustered lysosomes. Each line represents mean value from three independent experiments ± SEM. Percentage (scattered) = 23.5 ± 2.0, 6.4 ± 0.9, 3.5 ± 0.5, 0.9 ± 0.2, 0.2 ± 0.1, respectively, n= 29 embryos. Percentage (clustered) = 20.9 ± 2.9, 3.4 ± 0.7, 1.6 ± 0.5, 0.74 ± 0.2, 0.2 ± 0.1, respectively, n = 12 embryos.